Numerical Simulation of Wing-Fuselage Aerodynamic Interaction

J. S. Shang*
Air Force Wright Aeronautical Laboratories, Wright-Patterson Air Force Base, Ohio

Numerical solutions of the mass-averaged Navier-Stokes equations were accomplished for a wing-body configuration at a nominal Mach number of 6 and a Reynolds number of 15×10^6. The computations were performed on a CRAY-1 computer utilizing a grid consisting of 56,730 points. The wing-fuselage configuration is comprised of a tangent-ogive forebody and highly swept wedge delta wing. The present results, using a branch-cut mesh system, were verified by comparing with experimental measurements. An improvement in numerical resolution over the previous solution, utilizing a wraparound grid distribution, is clearly demonstrated. The flowfield structure is delineated by identifying the shock wave system and the cross-flow velocity field.

Nomenclature

c = speed of sound
def = deformation operator
D = Van Driest's damping factor
e = specific internal energy
F,G,H = vector fluxes
J = Jacobian of coordinate transformation
L = length scale of eddy-viscosity model
M = Mach number
n = outward normal
p = static pressure
Pr = Prandtl number, 0.72
Pr_t = turbulent Prandtl number, 0.9
r = radius of ogive forebody, 0.598 cm
Re = Reynolds number based on running length
T = temperature
U = dependent variables, $U(\rho,\rho u,\rho v,\rho w,\rho e)$
u,v,w = velocity components in Cartesian frame
x,y,z = coordinates in Cartesian frame
α = angle of attack
δ_{ij} = Kronecker delta
ϵ = eddy-viscosity coefficient
ξ,η,ζ = transformed coordinate
μ = molecular viscosity coefficient
ρ = density
τ = stress tensor
ω = vorticity vector

Subscripts

b = surface condition
0 = stagnation condition
∞ = freestream condition

Introduction

AERODYNAMIC interference around the juncture of the wing and fuselage is a direct consequence of three-dimensional inviscid and viscous interaction.[1-3] Until the early 1970s, numerical analyses for wing-body interference were exclusively restricted to small-disturbance schemes or panel methods.[1,2] In this mode of investigation, numerical analysis was used as an extension of analytic research. The uniqueness of the solution was ensured by imposing certain constraints such as the Kutta condition.[1] The achievement was very significant, however, directly usable results contained ambiguities. As computational aerodynamics made substantial progress, solutions of the quasilinear potential equation[4] and Euler equations became achievable.[5-7] The most recent efforts using the Euler equations which admit vorticity probably reflect the current state-of-the-art in solution development. However, the inviscid-viscous interaction around the wing-fuselage configuration remains unresolved.

In the past few years, numerical simulations of the wing-body combination by means of the parabolized and mass-averaged Navier-Stokes equations were attempted. In particular, Venkatapathy et al.[8] used a parabolized Navier-Stokes code to calculate the supersonic, viscous laminar flow around the Space Shuttle Orbiter forebody. Their solution contained the complex flow structure that developed near the wing-body region, and a multivortex pattern was observed. On the other hand, the present author also attempted to simulate numerically the flowfield around a hypersonic cruiser by means of the mass-averaged Navier-Stokes equations. Both investigations indicated that the local grid system played a very important role in resolving the flowfield around the wing-body juncture in that the geometric singularities were present. The appropriate selection of the coordinate system became critical. The main thrust of the current effort is to explore an alternative grid system.

The investigated wing-fuselage configuration is comprised of a tangent-ogive forebody and a sharp leading-edge delta wing with a sweepback angle of 70 deg (Fig. 1). The upper surface of the wing is mounted on the centerline of the fuselage, while the lower surface creates a 3-deg angle of attack with respect to the fuselage axis. Thus, the cross section of the wing-body retains only one axis of symmetry in the meridian place. The geometric singularities are consequences of joining piecewise continuous body surfaces at the wing-fuselage junction and the vanishing radius of curvature at the sharp leading edges of the wing tips. Locally, the homeomorphism cannot be maintained in the coordinate transformation to facilitate the computation. In the early effort, a wraparound coordinate system was adopted with some numerical rounding of the sharp edges. Basically, it was an H-O type grid which thus offered the most efficiency in terms of computational effort for a given resolution.[9] However, the H-O type grid around the wing tip caused serious numerical difficulties.[10] In the present analysis, a branch cut was incorporated for the body-oriented coordinate system. The mesh system can be identified as the H-H type (Fig. 2). The branch cut is performed along the upper and lower wing surfaces. The sharp wing tip is then contained within cells confined by nodes on the wing tip and the nodes immediately outboard to the leading edge. The singular points at the wing-fuselage juncture are defined precisely by the intersection of parametric lines (η,ζ). In particular, the

Presented as Paper 83-0225 at the AIAA 21st Aerospace Sciences Meeting, Reno, Nev., Jan. 10-13, 1983; submitted Feb. 2, 1983; revision submitted Nov. 22, 1983. This paper is declared a work of the U.S. Government and therefore is in the public domain.

*Aerospace Engineer. Associate Fellow AIAA.

coordinate system chosen essentially eliminates all of the geometric singularities of the wing-body configuration for the present numerical simulation.

Computations were performed for flowfields around a hypersonic cruise vehicle at a Mach number of 6.2 and a Reynolds number of 15×10^6. One of the computations was conducted for the flow without incidence; the other was perfomed for the oncoming stream with a 10-deg angle of attack. The present numerical effort investigates the intricate viscous-inviscid interaction around the wing-body configuration. In particular, the strong interactions present around the sharp apex of the fuselage and at the leading edge of the wing, and the possible flow separation region at the forward wing root area. At the simulated hypersonic Mach number, the computational domain is highly compact. For this case, a composite solution utilizing various approximations may not be the most cost-effective means of analysis. Thus, only the mass-averaged Navier-Stokes equations were used in the present analysis to predict the flow around a three-dimensional aircraft configuration and to assess the feasibility of full-scale numerical simulations. Special attention is focused on the treatment of the geometrical singularities frequently encountered in aircraft configurations. Thus, a criterion is established for the choice of coordinates for future full-scale aircraft numerical simulations. Numerical results are first verified by comparison with both static and impact pressure measurements under identical freestream conditions.[6] Then the flowfield structure is delineated by presenting the density contours, the cross-flow velocity distribution, and the streamwise vorticity formation.

Analysis

Governing Equations

The time-dependent, three-dimensional Navier-Stokes equations in mass-averaged variables and in the transformed space (ξ,η,ζ) can be given as[10]

$$\frac{\partial U}{\partial t}+(\xi_x,\xi_y,\xi_z)\begin{pmatrix}\frac{\partial F}{\partial\xi}\\ \frac{\partial G}{\partial\xi}\\ \frac{\partial H}{\partial\xi}\end{pmatrix}+(\eta_x,\eta_y,\eta_z)\begin{pmatrix}\frac{\partial F}{\partial\eta}\\ \frac{\partial G}{\partial\eta}\\ \frac{\partial H}{\partial\eta}\end{pmatrix}+(\zeta_x,\zeta_y,\zeta_z)\begin{pmatrix}\frac{\partial F}{\partial\zeta}\\ \frac{\partial G}{\partial\zeta}\\ \frac{\partial H}{\partial\zeta}\end{pmatrix}=0 \tag{1}$$

where the dependent variables are $U(\rho,\rho u,\rho v,\rho w,\rho e)$. The system is in the so-called chain rule conservation law form.[11,12] The Navier-Stokes equations in this particular form are more computationally efficient in comparison to both the strong and weak conservative forms.[12] The flux vectors F, G, and H are simply the Cartesian components of the continuity, momentum, and energy equations.

$$F=\Big[\rho u,\ \rho u^2-\tau_{xx},\ \rho uv-\tau_{xy},\ \rho uw-\tau_{xz}\ \rho eu-\gamma\Big(\frac{\mu}{Pr}+\frac{\epsilon}{Pr_t}\Big)\frac{\partial e}{\partial x}-(u\tau_{xx}+v\tau_{xy}+w\tau_{xz})\Big]^T \tag{2a}$$

$$G=\Big[\rho v,\ \rho uv-\tau_{yx},\ \rho v^2-\tau_{yy},\ \rho vw-\tau_{yz}\ \rho ev-\gamma\Big(\frac{\mu}{Pr}+\frac{\epsilon}{Pr_t}\Big)\frac{\partial e}{\partial y}-(u\tau_{yx}+v\tau_{yy}+w\tau_{yz})\Big]^T \tag{2b}$$

$$H=\Big[\rho w,\ \rho uw-\tau_{zx},\ \rho vw-\tau_{zy},\ \rho w^2-\tau_{zz}\ \rho ew-\gamma\Big(\frac{\mu}{Pr}+\frac{\epsilon}{Pr_t}\Big)\frac{\partial e}{\partial z}-(u\tau_{zx}+v\tau_{zy}+w\tau_{zz})\Big]^T \tag{2c}$$

where the component of shear stress is defined by

$$\tau_{ij}=(\mu+\epsilon)\,(\mathrm{def}\bar{u})_{ij}-[\tfrac{2}{3}(\mu+\epsilon)\,(\nabla\cdot\bar{u})+p]\delta_{ij} \tag{3}$$

The closure of the system of equations is achieved by introducing the Baldwin-Lomax turbulence model[13] with a minor modification and by assigning a turbulent Prandtl number of 0.9. Specifically the Baldwin-Lomax turbulence model is found to be Mach number dependent.[14] A constant in the outer layer is altered from a value of 1.5 to 2.0. The new constant (0.0336), twice the magnitude of Clauser's constant (0.0168), has been selected based on several benchmark calculations of turbulent flows over a flat plate at supersonic Mach numbers. For the skin friction coefficient prediction, the new constant used in the eddy-viscosity model results in a better agreement with experimental data. The two-layer eddy-viscosity model is given by

Inner region:

$$\epsilon=\rho(0.4LD)^2\,|\omega| \tag{4a}$$

where ω is the vorticity of the flowfield

$$\omega=\tfrac{1}{2}\nabla\times\bar{u} \tag{4b}$$

$$|\omega|=\tfrac{1}{2}\{[(\xi_y w_\xi+\eta_y w_\eta+\zeta_y w_\zeta)-(\xi_z v_\xi+\eta_z v_\eta+\zeta_z v_\zeta)]^2+[(\xi_z u_\xi+\eta_z u_\eta+\zeta_z u_\zeta)-(\xi_x w_\xi+\eta_x w_\eta+\zeta_x w_\zeta)]^2+[(\xi_x v_\xi+\eta_x v_\eta+\zeta_x v_\zeta)-(\xi_y u_\xi+\eta_y u_\eta+\zeta_y u_\zeta)]^2\}^{1/2}$$

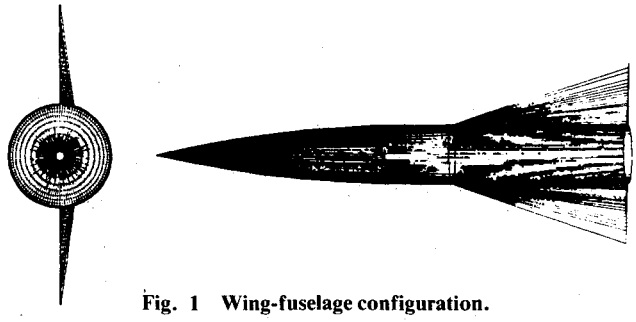

Fig. 1 Wing-fuselage configuration.

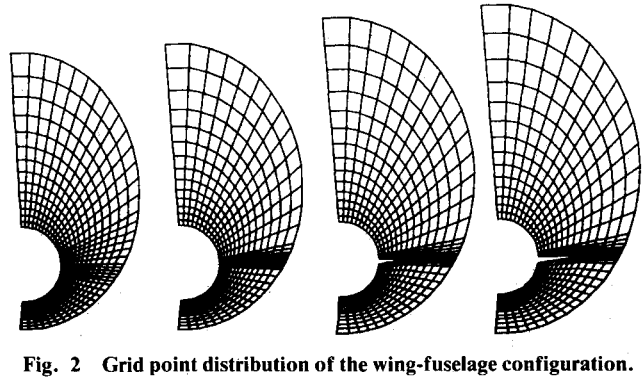

Fig. 2 Grid point distribution of the wing-fuselage configuration.

In the present formulation, the Van Driest damping factor D is given as

$$D=1-\exp\left[-\left(\frac{\rho_b|\omega_b|}{\mu_b}\right)^{1/2}L/26\right] \tag{4c}$$

In order to represent the appropriate turbulent shear layer structure (the laminar sublayer, the law of the wall, and the law of the wake regions), the description of the scaling length L is critical for the eddy-viscosity model. For the present analysis, an asymptotic length scale formula developed for an earlier investigation of a three-dimensional corner configuration is adopted for the wing-fuselage juncture region[11]:

$$L=2yz/[y+z+(z^2+y^2)^{1/2}] \tag{4d}$$

where y and z are the most natural Cartesian coordinates for describing the wing-fuselage juncture. Around the wing tip, the length scale is described by the radius of a cylindrical polar coordinate with the origin of the coordinate at the wing tip. This selection of scaling length permits a blending of the length scale from one region smoothly into the other.

Outer region:

The outer layer is basically the law of the wake including the intermittency correction by Klebanoff.[13]

$$\epsilon=0.0336\rho F_{\text{wake}}/[1+5.5(0.3L/L_{\max})^6] \tag{4e}$$

The wake function F_{wake} is given by the minimum value of the two following expressions at any point of interest in space.

$$F_{\text{wake}}=L_{\max}F_{\max} \tag{4f}$$

$$F_{\text{wake}}=0.25L_{\max}(u^2+v^2+w^2)_{\max}/F_{\max} \tag{4g}$$

In this case, $L_{\max}$ is the value of the length scale where $F=LD|\omega|$ reaches its maximum value within the turbulent shear layer. In the present formulation, the function F is dominated by the distribution of vorticity over the solid body contour. Thus, the continuous transition in the function F from the wing-fuselage junctions and the wing tip is ensured in the flowfield structure. The system of equations is formally closed with Sutherland's equation for molecular viscosity and the equation of state for a perfect gas.

The associated boundary conditions for the present investigation are straightforward. The initial condition is assigned the freestream value for the entire computational domain excluding only the surface nodes. On the solid body contour, the no-slip condition for velocity components, and the isothermal and orthoisobaric conditions are imposed for temperature and density, respectively. Since the attached bow shock wave isolates the interacting flow domain, the upstream and far-field conditions require that the flow remains unperturbed. For the oncoming stream with an angle of attack, the x and y components of velocity assign the values of $u_\infty\cos\alpha$ and $u_\infty\sin\alpha$, respectively, while the z component of velocity vanishes. The present analysis takes advantage of the property of symmetry with respect to the y axis (Fig. 2). Only a half cross-flow plane is evaluated at the plane of symmetry. A reflection condition is applied which insists that the z component of velocity be equal to zero. The usual no-change condition is imposed at the far downstream boundary. For the supersonic problem this boundary condition is known to be well posed and stable. In essence, we have:

Initial condition

$$U(0,\xi,\eta,\zeta)=U_\infty \tag{5a}$$

Upstream ($\xi=0$) and far-field condition ($\eta=1$)

$$U(t,0,\eta,\zeta)=u(t,\xi,1,\zeta)=U_\infty \tag{5b}$$

on solid contour

$$u,v,w=0 \tag{5c}$$

$$T_b=278\text{ K} \tag{5d}$$

$$\vec{n}\cdot\nabla p=0$$

where

$$\vec{n}=\nabla(x_b,y_b,z_b)/\|\nabla(x_b,y_b,z_b)\| \tag{5e}$$

Symmetry condition ($\zeta=0$, $\zeta=1$)

$$\frac{\partial U}{\partial\zeta}=0, \qquad w=0 \tag{5f}$$

Downstream condition ($\xi=1$)

$$\frac{\partial U}{\partial\xi}=0 \tag{5g}$$

Coordinate System and Grid Generation

The numerical generation of the body-oriented coordinate imposes serious difficulties for a wing-body configuration. The piecewise continuous segments of the body contour pose fundamental problems at the wing-fuselage juncture and wing tip. The geometric singularities will generate a vanishing Jacobian in the coordinate transformation. The one-to-one coordinate transformation cannot be maintained. As a common practice in numerical simulations,[5-8,10] small but finite fillets are incorporated to allow the transition from body to wing without significantly disturbing the flow. However, one cannot make the same statement for the sharp leading-edge wing tip. For inviscid analyses, this geometry-induced singularity can be resolved only through an asymptotic analysis[5] or by imposing the Kutta condition.[1] Therefore, the leading-edge singularity is excluded from the calculation. However, for the Navier-Stokes solution, the wing tip must be included in the computation and treated as a boundary point.

For the present investigation, in spite of the highly swept wing, the leading edge is still supersonic. Thus, numerically rounding the wing tip will alter the shock structure from an attached shock wave to a bow shock wave.[10] Meanwhile, the rapid metric variations around the wing tip cannot be eliminated completely. A better choice of coordinate systems becomes necessary. A new coordinate system with a branch cut along the wing surface may alleviate the difficulty. Steger and Bailey[15] used the C-type grid to investigate the transonic aileron buzz problem. Recently, Newsome[16] also successfully adopted a branch cut to accommodate the sharp cowl lip in his work on steady and oscillatory inlet flows. Particularly, in view of the fact that the leading edge of the wing in the limit sharpens to a cusp, the coordinate system with a branch cut can describe this unique characteristic easily. In essence, branch cuts are performed along the upper and lower wing surfaces and the cuts are extended to the outer boundary of the mesh system (Fig. 2). The branch cuts are defined by the constant values of the transformed coordinate ζ. The spacing between the cuts also represents the finest in the present calculations ($DY_{\min}=0.00012$ cm). The wing tip then is defined by the surface nodes and the immediately adjacent nodes upstream of the leading edge. Basically, the branch cuts remove all of the geometric singularities at the wing tip and wing-fuselage junctures. However, the solid contour of the wing-body configuration no longer lies on a single family of the transformed coordinate η. Additional logic control must be implemented in the vectorized code[10] to enforce the surface boundary conditions. It is obvious that the demanding

numerical resolution for a complex three-dimensional configuration will require the grid generation and the solving scheme to be tightly integrated in the future.

The necessary but tedious preparation of the mesh-point distribution for the rather complex wing-fuselage configuration is provided by a body-oriented homotopy scheme.[17,18] The coordinate system is constructed by a series of consecutive axial cross sections in the ξ direction unevenly spaced to achieve optimal numerical resolution. The leading plane is located upstream of the apex of the ogive forebody to facilitate the description of the unperturbed freestream. In each cross-sectional plane, a two-dimensional grid system is established between two control surfaces. The inner surface (Y_i, Z_i) depicts the body contour. The outer surface (Y_o, Z_o) is chosen to represent the enveloping shock wave. For the oncoming flow without incidence, the outer surface is a circle. Similarly, for the case of 10-deg angle of attack, the outer surface is described by an ellipse with an eccentricity of 1.10. The clustering of grid points adjacent to the solid body contour to account for the shear layer is attained by a self-adjusting stretching function. The field points are generated by the interpolation functions:

$$Y = Y_o\left(\frac{e^{k\eta}-1}{e^k-1}\right) + Y_i\left(1-\frac{e^{k\eta}-1}{e^k-1}\right) \tag{6a}$$

$$Z = Z_o\left(\frac{e^{k\eta}-1}{e^k-1}\right) + Z_i\left(1-\frac{e^{k\eta}-1}{e^k-1}\right) \tag{6b}$$

The numerically controlled mesh clustering is exercised only in the η coordinate which is nearly parallel to the body surface outward normal. The peripheral mesh spacing in ζ is explicitly described in the control surface coordinates (Y_i, Z_i and Y_o, Z_o). Since the rather complex three-dimensional body consists of two distinct geometric formations, the inverted wedge wing and the ogive forebody, the orthogonality of coordinates is not enforced. However, along the branch cut the coordinate is merely a mild deviation from the Cartesian frame. The single homotopy scheme is extremely efficient. Grid systems of $31\times30\times61$ points have been generated and evaluated on a CRAY-1 computer in less than 2 s. Once the coordinates X, Y, Z are generated, the derivatives of coordinate transformation can be evaluated through the Jacobian and its inverse.

Solving Scheme and Numerical Procedure

MacCormack's[19] explicit and unsplit algorithm is utilized in the present study to reduce the number of accessions of main memory, thereby developing an efficient data flow of the coding for a vector processor (CRAY-1). For a three-dimensional factored scheme, a field point requires five accessions of main memory in order to advance one time step in either the predictor or corrector sweep.

$$U^{n+1} = L_\zeta(\Delta t/2)\,L_\eta(\Delta t/2)\,L_\xi(\Delta t)\,L_\eta(\Delta t/2)\,L_\zeta(\Delta t/2)\,U^n \tag{7a}$$

However, the unsplit algorithm requires only one accession of main memory to acquire the same end result:

$$U^{n+1} = [L_\xi(\Delta t) + L_\eta(\Delta t) + L_\zeta(\Delta t)]\,U^n \tag{7b}$$

In the CRAY-1 computer, which operates on a single memory path, saving on memory loading is substantial. The present effort also indicates that the achievable data processing rate is 4.9×10^{-5} (seconds/grid points/time step) at a maximum vector length of 61. In comparison with an earlier effort,[20] the current development achieves a 20% improvement in the data processing rate. Vector processors such as the CRAY-1 and CYBER 203 make the reliable but conditionally stable MacCormack explicit method attractive.

In order to increase the capacity of data point processing in the vectorized code, the nine components of the coordinate transformation derivatives are computed at each node as needed without allocating storage space. Therefore, only the five dependent variables $U(\rho,\rho u,\rho v,\rho w,\rho e)$, three independent variables (x,y,z), and the eddy-viscosity coefficient (ϵ) are stored. The predictor-level variables are stored only for four consecutive streamwise pages in cyclic fashion. The temporarily stored information is replaced when numerical sweeps pass from page to page. This memory-saving procedure degrades the data processing rate. The startup times of vector registors and data movements have contributed up to 48% of the total computing time. This becomes apparent when the vectorized code is operating in the axisymmetric mode where all the temporary variables are computed for repeated usage. The data processing rate is reduced to 1.95×10^{-5} (seconds/grid/time step).[21] However, total of 56,730 points is accommodated by the CRAY-1 computer with 10^6 word memory. The new vectorized code[10] was initially developed on a CDC 175 computer, than transported and processed on a CRAY-1 computer. The ratio of data processing rates of the same code between the scalar and vector computer is 48:1.

In order to achieve maximum efficiency, the CFL condition on allowable time increment for generalized coordinates has been derived from a previous stability analysis.[10]

$$\Delta t_{\mathrm{CFL}} = 1\Big/\left\{u_\xi/\Delta\xi + u_\eta/\Delta\eta + u_\zeta/\Delta\zeta + c\left[\left(\frac{\xi_x}{\Delta\xi}+\frac{\eta_x}{\Delta\eta}+\frac{\zeta_x}{\Delta\zeta}\right)^2 + \left(\frac{\xi_y}{\Delta\xi}+\frac{\eta_y}{\Delta\eta}+\frac{\zeta_y}{\Delta\zeta}\right)^2 + \left(\frac{\xi_z}{\Delta\xi}+\frac{\eta_z}{\Delta\eta}+\frac{\zeta_z}{\Delta\zeta}\right)^2\right]^{1/2}\right\} \tag{7c}$$

where the contravariant velocity components are defined as

$$u_\xi = \xi_x u + \xi_y v + \xi_z w \tag{7d}$$

$$u_\eta = \eta_x u + \eta_y v + \eta_z w \tag{7e}$$

$$u_\zeta = \zeta_x u + \zeta_y v + \zeta_z w \tag{7f}$$

Since the stability analysis does not contain viscous terms, the highest and most consistent CFL number used is 0.85.

For the case of 10-deg angle of attack, the static pressure jumps fivefold across the shock wave system. Numerical

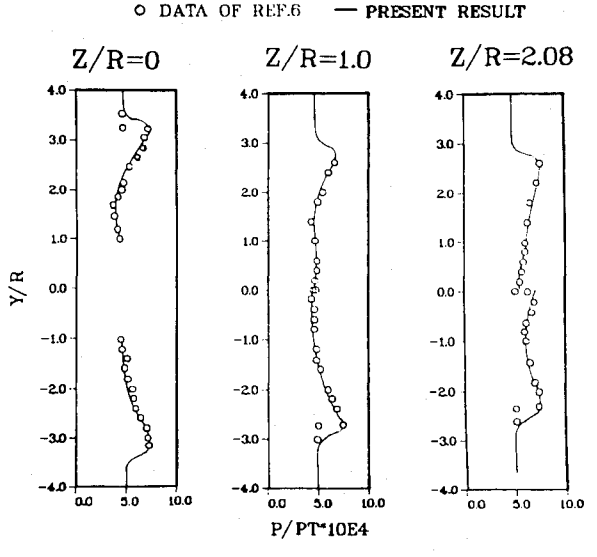

Fig. 3 Comparison of the static pressure distributions; $\alpha=0$, $x/r=13.15$.

damping is required to suppress numerical oscillations, thus MacCormack's fourth-order pressure damping terms are used with modification.[10,19] In essence, artificial viscosity-like terms are implemented in each sweep direction of the form

$$\beta\Delta t\Delta_\xi^3 [\,|u_\xi| + (\xi_x^2+\xi_y^2+\xi_z^2)^{1/2} c]\frac{1}{p}\left|\frac{\partial^2 p}{\partial \xi^2}\right| \tag{7g}$$

$$\beta\Delta t\Delta_\eta^3 [\,|u_\eta| + (\eta_x^2+\eta_y^2+\eta_z^2)^{1/2} c]\frac{1}{p}\left|\frac{\partial^2 p}{\partial \eta^2}\right| \tag{7h}$$

$$\beta\Delta t\Delta_\zeta^3 [\,|u_\zeta| + (\zeta_x^2+\zeta_y^2+\zeta_z^2)^{1/2} c]\frac{1}{p}\left|\frac{\partial^2 p}{\partial \zeta^2}\right| \tag{7i}$$

The result is identical to MacCormack's original expression if the Cartesian coordinate system were used. In the present analysis, the damping constant is limited to the range of values from two to three. These damping terms are only of significant magnitude in regions of pressure oscillation where the truncation error is already degrading the computations. The guiding line for the use of the damping term is simple: use sparingly and use only the bare minimum value to ensure the numerical evolution.

The solution is considered to be converged when the wing surface pressure variation is less than 2% over one-half of an elapsed characteristic time (U_∞/L). A total of 1.4 h of CRAY-1 computer time was required to meet the aforementioned criterion for $\alpha=0$. At the 10-deg angle of attack, the viscous effects became dominant as the inviscid-viscous interaction intensified. A significant reduction in allowable time step forces additional iterations to be performed to meet the convergence criterion. However, for the 10-deg angle-of-attack case, the initial condition is the converged case for $\alpha=0$. In this manner the 10-deg case required only 40% more total computing time to reach the steady asymptotic state.

Discussion of Results

The present results are given in three groups. In the first group of results, the numerical solution of flow without incidence is presented and compared with experimental data under identical flow conditions. The second group of results contains the validation and comparison with experimental data for 10-deg angle of attack. The rest of the discussion concentrates on the delineation of the detailed flow structure around the wing-fuselage configuration at 10-deg angle of attack.

The comparison of static pressure distributions around the wing-body combination at a distance of $x/r=13.15$ downstream of the apex of the ogive forebody is given in Fig. 3. The six sets of experimental data[6] were collected by surveying data along the y coordinate at various z coordinate locations. The values of $z/r=0$, 1.0, and 2.08 indicate locations of the meridian plane of the fuselage, the wing-fuselage juncture, and the wing tip of the wing-body combination, respectively. The configuration is not symmetric about the y axis due to the inverted wedge wing. The upper wing surface ($y\geq 0$) is parallel to the freestream; the lower wing surface ($y<0$) has a 3-deg incidence with respect to the oncoming stream. In spite of the 70-deg sweepback angle, the leading edge of the wing is supersonic, except perhaps a small portion of wing embedded in the viscous domain. Very good agreement between the data and the numerical results is observed. The maximum deviation between data and numerical results occurred in the definition of the bow shock wave region. Since this shock-capturing technique requires at least three points to define a finite pressure jump, the numerical smearing in the coarse mesh domain thus is unavoidable. Nevertheless, all essential features including the pressure jump across the bow shock wave are faithfully duplicated. Excluding the bow shock wave envelope due to numerical smearing, the maximum difference between data and calculations is confined within a few percent.

In Fig. 4, comparisons of pitot pressure distributions with data at locations identical to those of the static pressure profiles are presented. The pitot pressure is normalized with the freestream stagnation pressure $p_{t\infty}(4.1368\times10^3$ kPa). Thus the normalized pitot pressure attains a value of 0.027 in the freestream. The overall comparison of the data[6] with the present result is reasonable. The maximum discrepancy between data and present results is around 14% (mostly in the region bounded by the upper wing surface and fuselage). The experimental measurements revealed a much stronger expansion inboard of the wing tip than computations including the inviscid results[6] for the same configuration. However, both the data and numerical results indicate a larger stagnated region in the upper wing-fuselage juncture ($y/r>0$, $z/r=1$) than the lower juncture ($y/r<0$, $z/r=1$). A rapid expansion jet-like zone at the lower wing tip is also indicated.

The comparison of static pressure profiles at the 10-deg angle of attack is given in Fig. 5. The static pressure data were collected at a distance of $x/r=13.15$ downstream of the apex of the forebody. A set of pressure data was recorded in the meridian plane of fuselage ($x/r=0$). A pressure survey was conducted around the half-span of the leeward wing

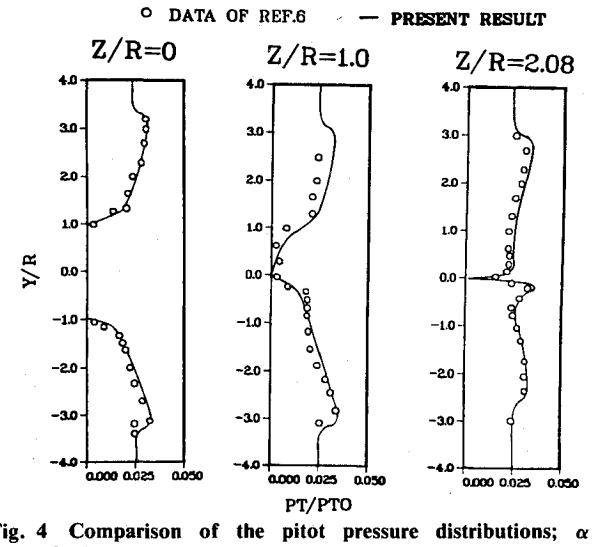

Fig. 4 Comparison of the pitot pressure distributions; $\alpha=0$, $x/r=13.15$.

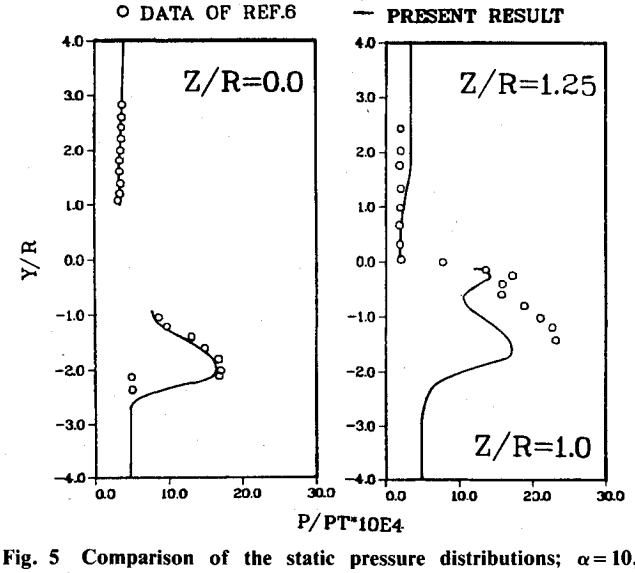

Fig. 5 Comparison of the static pressure distributions; $\alpha=10$, $x/r=13.15$.

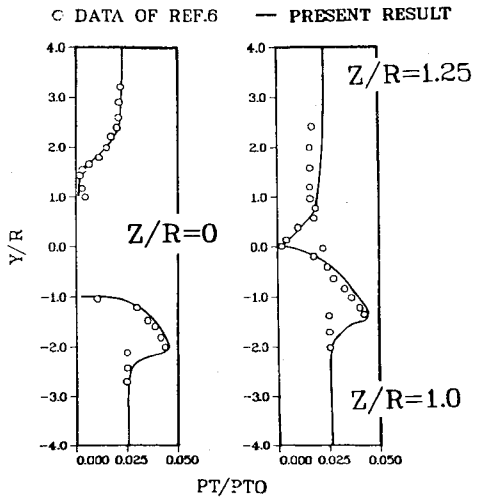

Fig. 6 Comparison of the pitot pressure distributions; $\alpha = 10$, $x/r = 13.15$.

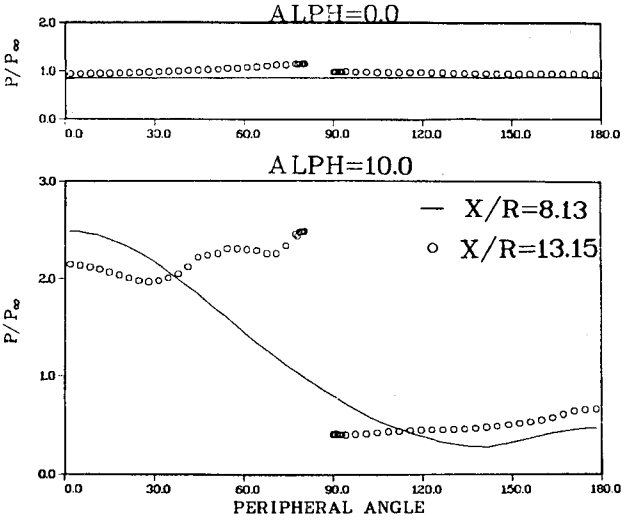

Fig. 8 Peripheral pressure distributions over the wing-body surface.

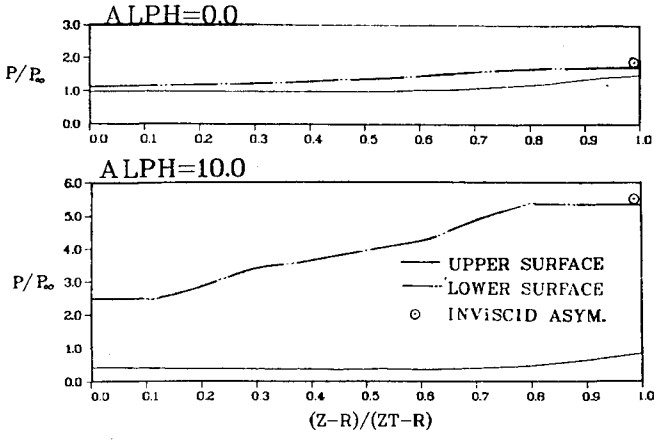

Fig. 7 Pressure distributions over the wing span.

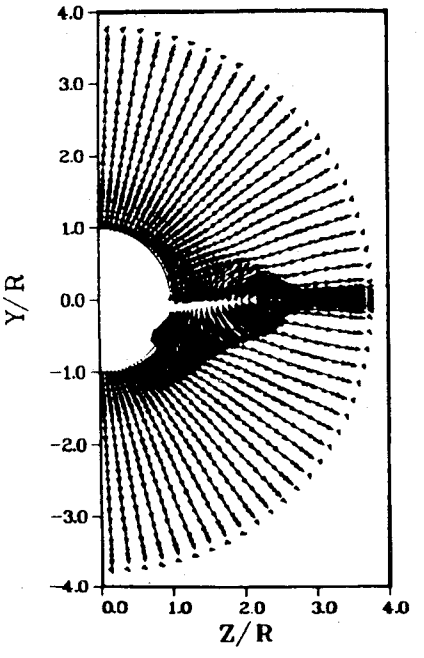

Fig. 9 Computed cross-flow velocity field of the wing-fuselage configuration; $\alpha = 0$, $x/r = 13.15$.

($x/r = 1.25$). In the windward domain, the only data collected were along the wing-fuselage juncture. Excellent agreement between data and calculation is obtained in the meridian of the fuselage. However, in the interacting zone a serious discrepancy between data and present results is revealed. According to the test record,[6] the static pressure probe was misaligned with the flow at high angle of attack. Thus it may be the cause of this observed difference. Again one must appreciate the extreme difficulty in acquiring accurate static pressure measurements in the strong viscous-inviscid interaction region. Nevertheless, the present result follows the general trend of the experimental measurement in the windward wing-fuselage juncture as it should.

In Fig. 6, the comparison of total pressure profiles at the exact survey stations to that of the static pressure distributions is presented. The pitot pressure probe is known to be relatively insensitive to the probe alignment with the flow. Excellent agreement between data and present results is clearly evident. Except perhaps in the shock envelope region, the deviation between data and present results is about the range of the data scattering. In short, the specific comparisons of static pressure distributions and pitot pressure profiles indicate that the present results duplicate nearly all the experimental measurements.

The static pressure distributions over the entire span of the wing surface at the 0- and 10-deg angles of attack are presented in Fig. 7. Numerical predictions at the wing tip and the meridian plane of fuselage agree very well with the inviscid asymptotes. For the flow without incidence, the upper surface pressure maintains the freestream value until about 0.8 of the wing span and then increases its value toward the wing tip. This pressure rise is due mainly to the classic pressure interaction induced by the displacement of the shear layer over the wing surface near the leading edge. The influence of pressure crossfeeding over the wing leading edge through the thin shear layer between the leeward (upper) and windward (lower) surfaces is rather limited. It is evident that the pressure jump across the wing tip is always maintained for both cases investigated. For the lower wing surface a continuous compression toward the wing tip originates at about 0.7 of the wing span. In the lower wing-tip region, the surface pressure attains the value equal to the oblique shock of 3-deg flow deflection. At 10-deg angle of attack, the pressure distributions over the wing exhibit a similar behavior. The only difference is that at the higher angle of attack, the windward surface pressure distribution reveals three plateaus. The lowest pressure plateau is in the wing-body juncture, then

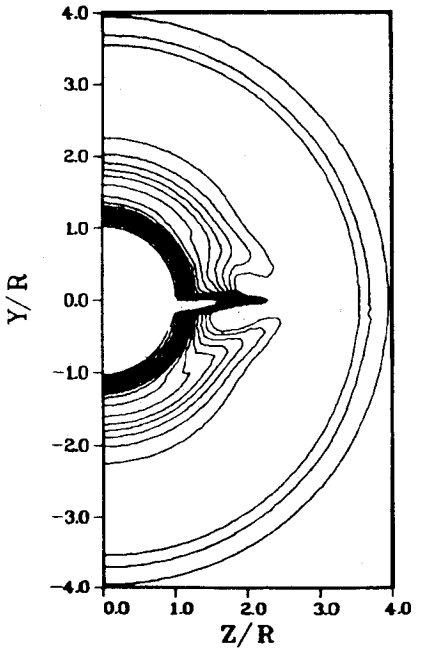

Fig. 10 Density contour over the wing-fuselage configuration; $\alpha = 0$, $x/r = 13.15$.

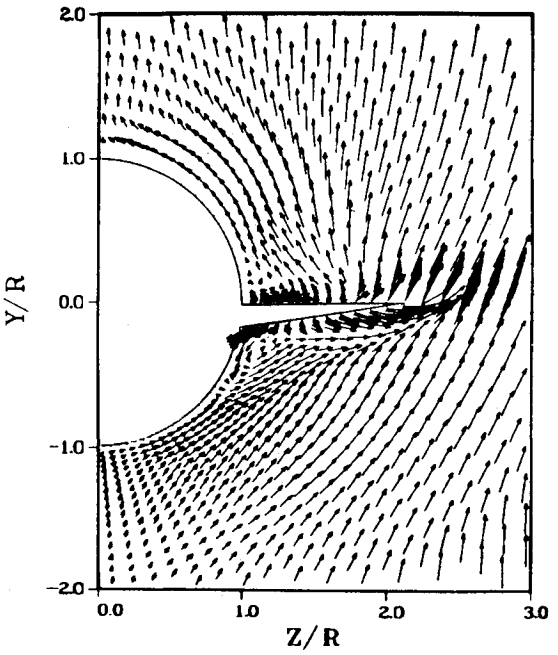

Fig. 12 Computed cross-flow velocity field of the wing-fuselage; $\alpha = 10$, $x/r = 13.15$.

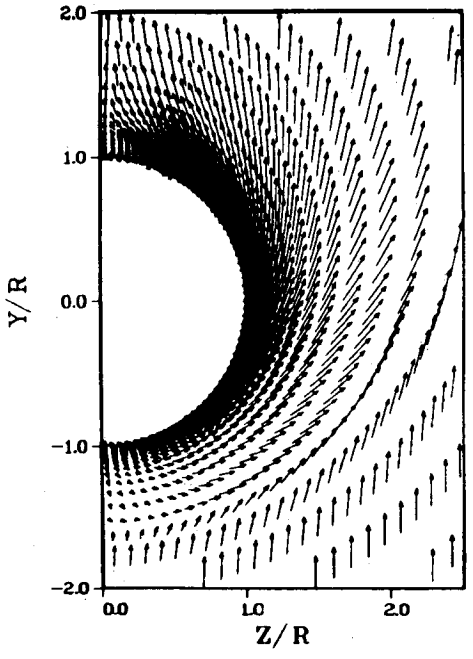

Fig. 11 Computed cross-flow velocity field of the cylindrical forebody; $\alpha = 10$, $x/r = 8.13$.

compresses rapidly to the midspan to reach the second pressure plateau and a final compression toward the wing tip. In the windward leading-edge domain, the surface pressure corresponds to the oblique shock value of 13-deg flow deflection. The expansion from wing tip to wing root over the windward domain substantially reduces the lift generated by the wing.

In Fig. 8, the circumferential surface pressures of the wing-body combination are presented. In addition, the circumferential surface pressure over the cylindrical forebody is also depicted here for reference purposes. This particular cross-flow plane is in the intermediate streamwise location between the ogive forebody and the plane where the wing is first merged with the fuselage. The circumferential pressure is similar to the pressure distribution over a circular cone at angle of attack.[22] For all of the cases considered, the aerodynamic interference in terms of pressure is unfavorable; the leeward pressure is higher and the windward pressure is lower than the forebody alone. Favorable interference is noted in both the leeward and windward wing-body junctures. However, the total contribution to the lift is small. Therefore, the present result at a Mach number of six shows an unfavorable aerodynamic interference for the delta-wedge wing and ogive cylindrical fuselage. The conclusion is consistent with the experimental observations that the compressibility effect and angle of attack reduce the wing-body interference factor from favorable to adverse.[5,23]

The flowfield of the wing-body at $\alpha = 0$ is described by a typical cross section contained wing-body combination. In Fig. 9, the cross-flow velocity field in the Cartesian frame is depicted. The bow shock wave is clearly revealed by the vanishing cross-flow velocity components outside the shock. An orderly displacement effect due to the wing is manifested and propagated over the interior domain. The leading-edge shock is attached, therefore the upwash around the wing tip is not discernible. The accompanying density contour is presented in Fig. 10. At this streamwise location, the bow shock is located 3.70 radii away from the axis of the fuselage. In spite of the presence of wing and the associated viscous-inviscid interaction, the enveloping bow shock seems to be free of serious distortion. The elusive leading-edge shock wave (which the earlier effort[10] utilizing a wraparound grid system cannot ascertain) stands out. In essence, the leading-edge shock and its attenuation toward the fuselage dominates the flowfield. The development of boundary layers on wing and fuselage surfaces is also obvious.

In order to describe the kinematic structure of the flow over the wing-fuselage at 10-deg angle of attack, the cross-flow pattern depicting w and v velocity components is given in Figs. 11 and 12. In Fig. 11, the vortical singularity liftoff and the flow separation over the leeward side of the forebody are clearly demonstrated. The line of flow separation is at a peripheral location of $\phi = 150$ deg, which is in perfect agreement with experimental observation.[6] In Fig. 12, the cross-flow velocity distribution over the wing-body combination is given. The flow separation in the windward junction of the wing and fuselage is clearly indicated. Along

the windward wing and outboard of the reattachment, a jet-like stream is observed. The presence of a leading-edge shock wave is also made evident by the abrupt change in orientation of the cross-flow velocity. Since the leading edge is supersonic, the shock wave is attached to the leading edge. No significant upwash around the wing tip is detected. Over the leeward wing-fuselage juncture, the recirculated separated flow is easily detectable. The stream liftoff over the leeward wing surface is also obvious. This phenomenon is faithfully depicted around 0.8 of the wing span. From the cross-flow velocity component, it is easily deduced that a multiple vortex structure exists in the cross-flow plane with strong concentrations at both the windward and leeward wing-body junctures, the leeward midspan of the wing, and over the leeward fuselage. All of these observations, in general, agree with experimental results. Unfortunately, no quantitative experimental record was available from the test,[6] Therefore, a specific comparison is not possible.

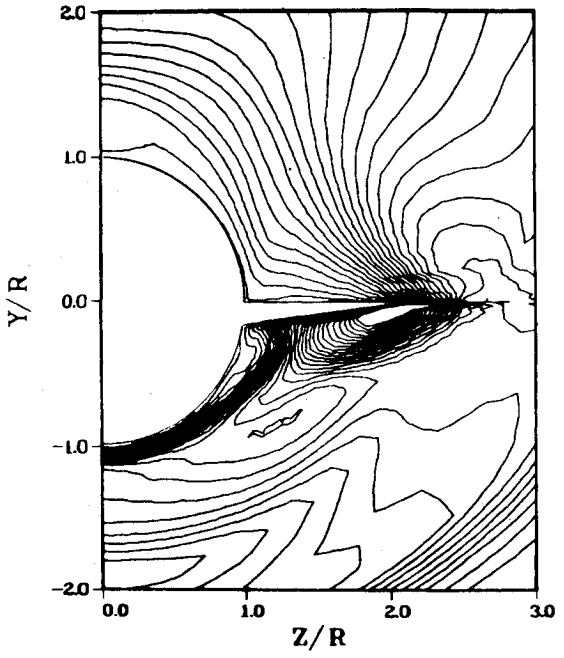

Fig. 13 Density contour over the wing-fuselage in the near field; $\alpha = 10, x/r = 13.15$.

An enlarged and isolated density contour at the streamwise location of $x/r = 13.15$ is presented in Fig. 13. In the windward region of the wing-fuselage configuration the outstanding feature is the leading-edge shock wave system and its attenuation toward the wing root. The shock wave structure is strongly influenced by the rapid circumferential expansion from the windward meridian to the wing-body juncture. In the present case, the pressure ($p/p_\infty = 5.23$) generated by the leading-edge shock is far greater than the pressure value ($p/p_\infty = 2.5$) in the wing-body juncture. Nevertheless, in the embedded juncture, the flow structure resembles that of an unsymmetric three-dimensional corner.[24] In the leeward domain, the flowfield is dominated by the rapid peripheral expansion. The flow structure in the wing-fuselage juncture is also overwhelmed by the expansion process.

In the final figure, density contours ranging from the ogive forebody to the wing-body combination are selectively presented in Fig. 14. Two features stand out in this figure, namely, the growth of the enveloping bow shock wave and the distortion of the bow shock due to the wing. The density contours upstream of wing bear the strong resemblance to that of conical flow at an angle of attack.[2] The windward bow

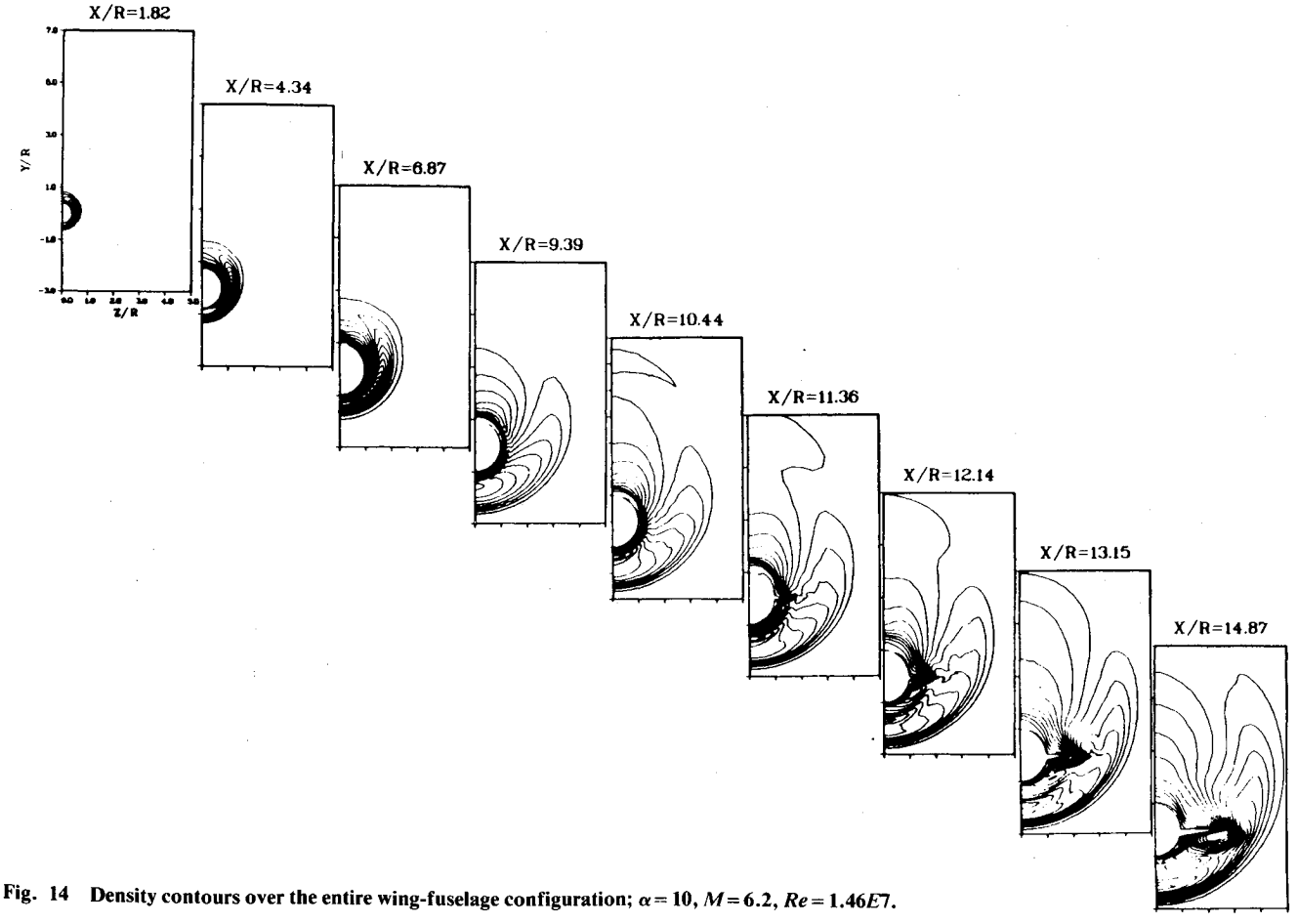

Fig. 14 Density contours over the entire wing-fuselage configuration; $\alpha = 10$, $M = 6.2$, $Re = 1.46E7$.

shock dominates, then the flow expands rapidly leeward into the aerodynamic shadow. As soon as the wind merges from the fuselage the leading-edge shock appears in the windward domain and overwhelms all other features of the flow.

Concluding Remarks

The numerical solutions of Navier-Stokes equations were accomplished for flowfields around a wing-fuselage configuration at a Mach number of 6.2 and a Reynolds number of 15×10^6. The numerical simulations were successful for the flow without incidence and at 10-deg angle of attack. The aerodynamic interference of the ogive cylindrical fuselage and the inverted wedge delta wing was found to be unfavorable.

The selection of a coordinate system for a configuration containing geometric signularities is shown to be critical. From the topological point of view, the adoption of a branch-cut or wraparound system (C- or O-type grid) is immaterial. However, the metric variation around the geometrically induced singularities will determine the success or failure of the numerical simulation. Therefore, the grid generation and the solving procedure cannot be treated as separate issues. This finding is paramount in our pursuit to simulate the full-scale aircraft by means of segmented or patched computational domains in the near future.

References

[1] Ashly, H. and Rodden, W. P., "Wing-Body Aerodynamic Interaction," *Annual Review of Fluid Mechanics*, Vol. 4, 1972, pp. 431-472.

[2] Loeve, W., "The Calculation of Aerodynamic Characteristics of Wing-Body Combinations at Subsonic Flight Speeds," *Lecture Notes in Physics*, Vol. 59, 1976, p. 75.

[3] Peake, D. J. and Tobak, M., "Three-Dimensional Interactions and Vortical Flows with Emphasis on High Speeds," AGARDograph 252, July 1980.

[4] Caughey, D. A. and Jameson, A., "Numerical Calculations of Transonic Potential Flow About Wing-Body Combinations," *AIAA Journal*, Vol. 17, Feb. 1979, pp. 175-181.

[5] Klopfer, G. H. and Nielson, J. H., "Euler Solutions for Wing and Wing-Body Combination at Supersonic Speeds with Leading-Edge Separation," AIAA Paper 80-0126, Pasadena, Calif., Jan. 1980.

[6] Wang, C. R., Zakkay, V., and Parikh, H., "An Experimental and Analytical Investigation of a Hypersonic Cruising Vehicle at Mach 6," AIAA Paper 80-0004, Pasadena, Calif., Jan. 1980.

[7] Rizzi, A., "Damped Euler-Equation Method to Computer Transonic Flow Around Wing-Body Combinations," *AIAA Journal*, Vol. 20, Oct. 1982, pp. 1321-1328.

[8] Venkatapathy, E., Rakich, J. V., and Tannehill, J. C., "Numerical Solution of Space Shuttle Orbiter Flow Field," AIAA Paper 82-0028, Orlando, Fla., Jan. 1982.

[9] Eriksson, L. E., "Generation of Boundary-Conforming Grids Around Wing-Body Configurations Using Transfinite Interpolation," *AIAA Journal*, Vol. 20, Oct. 1982, pp. 1313-1320.

[10] Shang, J. S., "Numerical Simulation of Wing-Fuselage Interference," AIAA Paper 81-0048, St. Louis, Mo., Jan. 1981.

[11] Shang, J. S., Hankey, W. L., and Petty, J. S., "Three-Dimensional Supersonic Interacting Turbulent Flow Along a Corner," *AIAA Journal*, Vol. 17, July 1979, pp. 706-713.

[12] Hindman, R. G., "Generalized Coordinate Forms of Governing Fluid Equations and Associated Geometrically Induced Errors," *AIAA Journal*, Vol. 20, Oct. 1982, pp. 1359-1367.

[13] Baldwin, B. S. and Lomax, H., "Thin Layer Approximation and Algebraic Model for Separated Turbulent Flows," AIAA Paper 78-257, Huntsville, Ala., Jan. 1978.

[14] Knight, D. D., "Hybrid Explicit-Implicit Numerical Algorithm for the Three-Dimensional Navier-Stokes Equations," AIAA Paper 83-0223, Reno, Nev., Jan. 1983.

[15] Steger, J. L. and Bailey, H. E., "Calculation of Transonic Aileron Buzz," AIAA Paper 79-0134, New Orleans, La., Jan. 1979.

[16] Newsome, R. W., "Numerical Simulation of Near-Critical and Unsteady Subcritical Inlet Flow Fields," AIAA Paper 83-0175, Reno, Nev., Jan. 1983.

[17] Eiseman, P. R. and Smith, R. E., *Mesh Generation Using Algebraic Techniques*, NASA CP 2166, Oct. 1980, pp. 73-120.

[18] Shang, J. S., Smith, R. E., and Hankey, W. L., "Flow Oscillations of Spike-Tipped Bodies," AIAA Paper 80-0062, Pasadena, Calif., Jan. 1980.

[19] MacCormack, R. W., "Numerical Solutions of the Interactions of a Shock Wave with Laminar Boundary Layer," *Lecture Notes in Physics*, Vol. 59, 1976, pp. 151-163.

[20] Shang, J. S., Buning, P. G., Hankey, W. L., and Wirth, M. C., "Performance of a Vectorized Three-Dimensional Navier-Stokes Code on the CRAY-1 Computer," *AIAA Journal*, Vol. 18, Sept. 1980, pp. 1073-1079.

[21] Hankey, W. L. and Shang, J. S., "Natural Transition—A Self Excited Oscillation," AIAA Paper 82-1011, St. Louis, Mo., June 1982.

[22] McRae, D. S. and Hunsami, M. Y., "Numerical Simulation of Supersonic Cone Flow at High Angle of Attack," *High Angle of Attack Aerodynamics*, AGARD-CP-247, Oct. 1978, pp. 23-1, 23-10.

[23] Nielsen, J. H., "Nonlinearities in Missile Aerodynamics," AIAA Paper 78-20, Huntsville, Ala., Jan. 1978.

[24] Shang, J. S. and Hankey, W. L., "Numerical Solution of the Navier-Stokes Equations for a Three-Dimensional Corner," *AIAA Journal*, Vol. 15, Nov. 1977, pp. 1575-1582.